2

3

Fabrication of Bioinspired Micro/Nano-Textured Surfaces Through Scalable Roll Coating Manufacturing

4	
5	Benjamin Black
6	North Carolina State University
7	Engineering Building III, 1840 Entrepreneur Dr., Raleigh, NC 27695.
8	bcblack6@ncsu.edu
9	
10	Sekkappan Chockalingam
11	North Carolina State University
12	Engineering Building III, 1840 Entrepreneur Dr., Raleigh, NC 27695.
13	schocka@ncsu.edu
14	
15	Md Didarul Islam
16	North Carolina State University
17	Engineering Building III, 1840 Entrepreneur Dr., Raleigh, NC 27695.
18	mislam9@ncsu.edu
19	
20	Sipan Liu
21	North Carolina State University
22	Engineering Building III, 1840 Entrepreneur Dr., Raleigh, NC 27695.
23	sliu46@ncsu.edu
24	
25	Himendra Perera
26	North Carolina State University
27	Engineering Building I, 911 Partners Way, Raleigh, NC 27695.
28	khperera@ncsu.edu
29	
30	Saad Khan
31	North Carolina State University
32	Engineering Building I, 911 Partners Way, Raleigh, NC 27695.
33	khan@ncsu.edu
34	
35	Jong Eun Ryu ¹
36	North Carolina State University
37	Engineering Building III, 1840 Entrepreneur Dr., Raleigh, NC 27695.
38	jryu@ncsu.edu

¹ Corresponding author. E-mail address: jryu@ncsu.edu

1

ABSTRACT

Bioinspired, micro/nano-textured surfaces have a variety of applications including superhydrophobicity, self-cleaning, anti-icing, anti-biofouling, and drag reduction. In this paper, a template-free and scalable roll coating process is studied for fabrication of micro/nano-scale topographies surfaces. These micro/nano-scale structures are generated with viscoelastic polymer nanocomposites and derived by controlling ribbing instabilities in forward roll coating. The relationship between process conditions and surface topography is studied in terms of shear rate, capillary number, and surface roughness parameters (e.g., Wenzel factor and the density of peaks). For a given shear rate, the sample roughness increased with a higher capillary number until a threshold point. Similarly, for a given capillary number, the roughness increased up to a threshold range associated with shear rate. A Peak Density Coefficient model is proposed to relate capillary number and shear rate to surface roughness. The optimum range of the shear rate and the capillary number was found to be 40-60 s⁻¹ and 4.5×10⁵- 6×10⁵, respectively. This resulted in a maximum Wenzel roughness factor of 1.91, a peak density of 3.94×10⁴ (1/mm²), and a water contact angle (WCA) of 128°.

INTRODUCTION

In nature, the application of micro/nanotextured surfaces include superhydrophobicity, self-cleaning, anti-icing, anti-biofouling, and drag reduction [1–6]. More specifically, these micro/nano surface topographies enable dragon fly wings to maintain a clean surface [7], geckos to adhere to branches [8], and water striders to travel on top of water [9]. One example in nature with a growing interest in the scientific community is the lotus leaf, which has micro papillae ($^{\sim}10~\mu m$ in diameter) that exist on the surface and are part of a dual hierarchial structure that enable superhydrophobic properties [10]. Researchers have successfully fabricated

67 microstructured surfaces replicating that of lotus leaves to achieve superhydrophobicity [10,11].

Superhydrophobic surfaces have a WCA above 150° and a hysteresis angle lower than 5° [12]. This phenomenon is often enabled by adding small protrusion-like textures on a surface. With a dense population of added textures, the spacings in between cannot be occupied by the liquid and instead, become filled with air. In this case, the wettability of the surface enters the Cassie-Baxter regime. In this regime, the WCA depends on the area of the surface that is in contact with the liquid. Thus, surface topography has an extreme effect on the wettability of the material surface. Some of the technologies utilized to fabricate these superhydrophobic surface topographies include photolithography, laser cutting, 3D printing, and nanoimprinting [13–17]. However, there are still overarching challenges including cost, manufacturing scalability, and durability. For example, photolithography, the most common method for producing such surfaces, is limited to small area substrates [18]. As a result, manufacturing a large area of a bioinspired surface is very challenging with this process.

To address these scalability issues, Park et al. utilized a two-roll coating method to fabricate micro and nano-scale 3-dimensional (3D), topographic surfaces [19]. The roll coating method successfully achieved hydrophobic surfaces in a scalable way; however, the process parameters (the viscoelastic properties of the coating materials, roll-coating speed, and shear rate) to engineer the surface morphology were not studied extensively.

The difficulty associated with scalable manufacturing of superhydrophobic surfaces has prompted the authors to investigate a common roll-to-roll manufacturing defect known as ribbing, in which spatially periodic patterns occur transverse to the roll-coating direction [20–23]. This defect is undesirable in common roll coating applications such as polymer thin films [24,25], painting [26,27], and flexography printing [28,29]. The ribbing is generated by a positive pressure gradient in the downstream meniscus of the coating fluid [30]. When this pressure gradient exceeds a critical value, a finger-like growth (ribbing) is observed [31,32]. While this phenomena is generally undesirable, controlling these ribbing patterns can assist in replicating microstructures with superhydrophobic properties that are obtained by the previously outlined methods.

The ribbing phenomena occurs in both Newtonian and non-Newtonian fluids, and it has been studied through experimental and computational models to mitigate its effect in roll-coating applications [20–23,33]. Prior research has demonstrated that the ribbing amplitude and wavelength ($\lambda_{Ribbing}$) have a strong relationship with process parameters, including the roller radius R, roller gap d, viscosity η , surface energy γ , and roller speed U, as well as material properties [31,32,34,35]. The onset conditions for ribbing in a Newtonian fluid can be described by two dimensionless parameters: the geometric factor R/d and the capillary number $C\alpha = \eta U/\gamma$. In Newtonian fluids, the critical Capillary number, Ca^* , showed a linear proportionality with the geometric factor [20,21,23,32,36,37]. It is important to note that the critical capillary number is much lower for non-Newtonian fluids than for Newtonian fluids [37]. Furthermore, the

theoretical prediction of the Ca^* in viscoelastic fluids is not obtainable; however, it can be obtained in Newtonian fluids.

In previous works, López et al. found a relationship between viscoelastic fluids and the critical capillary number. By controling the elasticity with a varying concentration of polymer molecules in a Newtonian fluid (Glycerol/Water), López et al. found similar trends in the Ca^* and the normal stress parallel to the flow as the concentration of the polymer increased [37]. Thus, these results imply that the viscoelastic fluid increased the stress in the flow direction by restricting the flow and causing the ribbing instability to occur at a slower roller speed or Capillary number. In addition to these findings, computational simulations performed by Zevallos et al. showed that at any given Ca there is a critical Weissenberg number (Wi) that dictates the threshold where the flow becomes unstable [30]. Prior research has focused on the identification of the critical Capillary number in non-Newtonian fluids; however, the fluid propagation and ribbing formation beyond these conditions have yet to be explored [22,38,39].

This study focuses on the physical properties of roll-coating pastes and how they influence ribbing instabilities to achieve scalable manufacturing of superhydrophobic surfaces that are similar to the surface topography of lotus leaves. When generating superhydrophobic surfaces using roll-coating, the ribbing patterns can flatten when the roller stops. This is due to the surface tension dominating over viscosity. It is critical to retain the ribbing pattern after the rollers stop in order to manufacture super

hydrophobic surfaces. This can be avoided by altering the coating fluids viscoelastic properties through nanoparticle addition [40–42].

MATERIALS AND METHODS

The nanocomposite material used in this study was synthesized by dispersing 10 wt % of multiwalled carbon nanotube (MWCNT, 10-nm diameter, and 100-µm length) in polydimethylsiloxane (PDMS) polymer. This non-Newtonian viscoelastic paste was mixed initially through a centrifugal planetary mixer. To ensure effective dispersion and homogenization of the highly entangled MWCNTs within the polymer matrix, a three-roll milling machine was used to perform mixing for approximately 30 mins.

A two-roll coating machine was then used to fabricate the textured samples. Two rollers with a diameter of 50.8 mm and a length of 300 mm were placed in parallel and the high viscosity CNT-PDMS polymer composite was placed between the rollers. The speed of the rollers can be independently varied from 0 to 120 rpm. A schematic of the two-roll coating machine is shown in Fig. 1. Here, V_1 is the velocity of roller 1 and V_2 is the velocity of roller 2. Roller 1 has a removable polyimide sleeve which is used to remove the sample after fabrication. Once the rollers begin rotation, the paste gets transferred onto the roller with a higher speed and is spread across the circumference of the roller as depicted.

In the study, initially, V_1 is held higher than V_2 when the paste is inserted. Thus, the paste is coated as a smooth film onto roller 1 as materials prefer to transfer to the roller with higher velocity. Then, V_2 is kept constant and V_1 is gradually reduced to be

below V_2 . When V_1 is less than V_2 , the coating paste on roller 1 demonstrates a capillary bridging phenomenon [10]. Here the coating paste is in contact with both rollers, but as the rollers keep rotating, the paste moves along with the rollers only to split shortly afterward due to the surface tension and capillary forces. This phenomenon creates micropatterns with high aspect ratios which can be observed in Fig. 1. After coating, the samples were cured at 125 °C for 25 mins.

The rheology properties of the 10 wt% CNT-PDMS composite paste, such as the apparent viscosity, storage modulus, and loss modulus were measured by a temperature-controlled rotational rheometer (TA Instruments Discovery Hybrid-3). The experiments were conducted with a 1000 μ m gap height, 8 mm cross-hatched steel plates, and a temperature of 25 °C. The amplitude sweep was conducted with 5×10^{-3} to 5 oscillation strain percentage at 1 Hz frequency. The frequency sweep was conducted at 0.03 strain percentage.

The 2D and 3D surface profiles were characterized by the non-contacting, laser-scanning, confocal microscope (Keyence VK-X1100, 0.5 nm height resolution, and 1 nm width resolution). A 20x lens was used to scan the surface of the sample with a total magnification of 480X. The multifile analyzer software was used to retrieve the results from the scanned image.

Detailed surface features were further analyzed by the Scanning Electron

Microscope (Field Emission Scanning Electron Microscope - Verios 460L). The resolution

of this equipment is 0.6 nm from 2 kV to 30 kV. The WCA of the samples were measured

in 5-8 locations per sample, using the contact angle goniometer. The average values of the WCA are reported in the study.

The surface energy was measured using the Owens-Wendt Model. Four different test liquids were used to measure the liquid contact angles on the surface. Based on the contact angle results, the Owens-Wendt model was plotted and the surface energy of the solid surface used was measured. From the conducted experiment, the surface energy, or the surface tension of 10 wt% CNT-PDMS was found to be 22.47 mJ/m².

RESULTS AND DISCUSSION

Rheology Property of the Paste

The viscosity of the composite paste reduces as the shear rate increases (Fig. 2(a)). This confirms that the non-Newtonian composite paste followed a shear thinning behavior. Storage Modulus (G') is defined as the measure of elasticity of the material. This is the ability of the material to store energy. The Loss Modulus (G'') is defined as the measure of the viscosity of the paste. This is the ability of a material to dissipate energy. These moduli were plotted for oscillatory strain to locate the Linear Viscoelastic Region (LVR). The stable moduli value for a range of oscillatory strains in Fig. 2(b) confirms the LVR for the 10% CNT – PDMS composite paste used in experimentation. It also demonstrates a satisfactory strain resistance before it yields. The viscoelastic behavior at the LVR is presented in Fig. 2(c). Fig. 2(c) plots the frequency sweep for the two moduli. It had a very linear trend without any fluctuations. It was also seen that the value of the storage modulus (G') is greater than the value of the loss modulus (G'').

Thus, the experiment confirmed that the composite paste has an elastic solid-like nature.

Experimental Design

A preliminary study was conducted to see how the composite paste behaved in our two-roll coating set-up. The roll coating experiment was established and the initial samples were fabricated with various roller speeds. The gap between the rollers was kept constant at 0.5 mm throughout the experiments. To clearly understand the effect of the process speeds and the composite paste property, two parameters were described. Shear rate is defined as the ratio between the difference of the two roller velocities and the gap between the rollers as shown in the equation. The capillary number (C_a) is defined as the product of viscosity and fluid velocity over the surface tension.

Shear rate =
$$\frac{|V_1 - V_2|}{d}$$
 (1)

$$C_a = \frac{\textit{Viscosity} \times \textit{Avg. Velocity}}{\textit{Surface Tension}} \tag{2}$$

The shear rate defines the effect of the process, while the capillary number defines the effect of the paste on the two roll coating experiments. Table 1 shows the process parameters and the surface morphology of the preliminary results. These process parameters were selected based on a literature survey and an experimental design was created by incrementing and decrementing the shear rate based on prior studies to obtain a process window [19,43]. Six samples A-F were fabricated in the preliminary study. Sample E was the only sample to show the desired rough-textured

surface. All other samples showed a smooth surface. The smooth surface was characterized through visual analysis of SEM imaging. The SEM used to determine whether a surface was smooth or rough can be found in Table 1. To better understand the results, the process parameters were plotted based on the surface roughness as shown in Fig. 3.

Fig. 3 shows the parameter plot used to finalize the process window for the fabrication of the samples. The shear rate was plotted for various samples in Fig. 3(a). The roughness designation is indicated by different colors. Sample E shows the roughest surface (red) with a shear rate of $42.56 \, \text{s}^{-1}$. It is seen that a shear rate below $80 \, \text{s}^{-1}$ always produces smooth surfaces. Also, if the shear rate is very low in magnitude (say $20 \, \text{s}^{-1}$), it might not be enough to produce rough surfaces. Thus, we attain an operable range for a shear rate of around $20 \, \text{s}^{-1}$ to $80 \, \text{s}^{-1}$.

A similar plot was made for the capillary number in Fig. 3(b). Sample E, the roughest surface (red) had a capillary number of 5.38×10^5 . It is seen that surfaces with capillary number approximately below 4×10^5 only produces smooth surfaces. While we are unaware of the upper limit of this capillary number for attaining the rough surface, it is concluded that it must possess a minimum capillary number for the rough textures to appear. It is also expected that there is a higher possibility to attain rough surfaces for a capillary number greater than 4.5×10^5 . In addition, to achieve a rough surface, the conditions for both the shear rate and the capillary number must be satisfied.

Based on the preliminary results, the parameters were selected from the defined process window. 4 levels of shear rate and 3 levels of the capillary number were used to

fabricate the samples. Thus, in this study 12 samples were fabricated and analyzed as documented in Table 2.

Surface Morphology Results

At a certain shear rate, a micro/nanostructured rough topography develops over the entire film area. The formation of this instability pattern is strongly related to the dynamic rheological property and the process parameters. Even after removing this shear stress, the deformed shape was retained due to the recovery of the high viscous non-Newtonian paste. A large yield shear stress of the polymer composite makes the composite behave like a solid in absence of shear stress.

Fig. 4 shows the SEM images of all 12 samples. A basic understanding of the samples was obtained using these SEM images. It was seen that the medium and high C_a samples were rougher than the low C_a samples. Also, samples with shear rates 42.56 s⁻¹ and 58.52 s⁻¹ showed rough surfaces compared to others. However, these images were compared with the surface descriptors obtained using the laser confocal data.

Surface Roughness Results

The relationship between the process conditions and the rough-textured surface characteristics was studied using the shear rate, capillary number, and the surface roughness descriptor. Basic roughness values like *Ra*, *Rq*, and *Rz* cannot describe both the horizontal and vertical roughness of the sample. To understand the overall roughness description of any sample, we need better descriptors that consider both the

267 2D and 3D texture of the surface. Two such descriptors used in this study are Wenzel roughness factor (*r*) and peak density (*Spd*).

Wenzel roughness factor is defined as the ratio of the Actual (textured) surface area to the cross-section area of the sample.

$$r = \frac{Actual \, Surface \, Area}{Cross \, Section \, Area} \tag{3}$$

The laser confocal Multifile analyzer software gives the Developed Interfacial Area Ratio (*Sdr*) of the sample. *Sdr* is defined as the difference between the Actual textured surface area and the footprint cross-section area over the footprint cross-section area.

$$Sdr = \frac{Actual Surface Area-Cross Section Area}{Cross Section Area}$$
 (4)

277 From this *Sdr*, the *r*-value can be obtained by adding 1 to it.

$$278 r = 1 + Sdr (5)$$

So, from the equation, it is obvious that a high value of r means that the roughness of the sample is also higher.

Peak density is the number of peaks in a given area. Here, the area is considered as 1 mm². Thus the number of peaks in a 1 mm² area is reported as *Spd*. This value is directly obtained from the Multifile analyzer software. Again, a high value of *Spd* means that the roughness of the sample is also higher.

The results from the laser confocal roughness measurement were obtained and documented in Table 3. The variation in the Wenzel roughness factor (r) with respect to the capillary number for various shear rates was plotted in Fig. 5 (a). It can be seen that the lowest and highest shear rate had a linear increasing trend. The r of the mid shear

range (40 - 60 s⁻¹) showed an initial increase and then decreased with an increase in C_a . A sample was considered as a good textured sample if the r value was greater than 1.5. From our results, we found that, for the r-value to be greater than 1.5, the range of the capillary number should be from 4.5 x 10⁵ to 6.0 x 10⁵, and the shear rate should be greater than 40 s⁻¹. Almost all of the samples that had a capillary number around 5 x 10⁵ and a shear rate greater than 40 s⁻¹ (Sample 2b, 3b, 4a) had a high r-value. The sample with high roughness and the textured surface was obtained with a shear rate of 42.56 s⁻¹ and a capillary number of 5.38 x 10⁵. All samples with a shear rate greater than 40 s⁻¹ have more than 10,000 peaks which guaranteed a minimum textured surface.

Fig. 5(b) shows the variation of peak density with the capillary number. The samples with mid- C_a showed high roughness in terms of the number of peaks. Samples with high capillary numbers showed an increasing trend, while other samples showed an initial increase in peak density and then decreased. All samples with a shear rate greater than 40 s⁻¹ have more than 10,000 peaks which guaranteed a minimum textured surface. Samples in the mid capillary number region showed higher peak density than other samples.

Fig. 6(a) shows the variation of the Wenzel roughness factor (r) with respect to the shear rate for various capillary numbers. It can be seen that the mid- C_a samples showed high r values. The samples with high C_a showed an increasing trend with respect to shear rate while the r-value of the low and mid C_a samples increased initially and then decreased. The reason for this was attributed to the decrease in viscosity. Similarly, Fig. 6 (b) shows the variation of the peak density with respect to the shear rate for various

capillary numbers. The low and mid C_a showed an initial increase and then a decrease in the peak density of the sample as the shear rate increased. The high C_a samples showed an increase in peak density as the shear rate increased. The sample with the highest shear rate (79.80 s⁻¹) and the highest C_a (5.38 x 10⁵) resulted in the highest peak density (3.94 x10⁴ mm⁻²).

The samples with high C_a showed an increasing trend of Wenzel roughness with shear rate. While on the other hand, the r of the low and mid C_a samples increased initially with shear-rate and then decreased. Since the paste is a shear-thinning fluid, the viscosity was inversely proportional to the shear rate. As the shear rate increased, the viscosity kept reducing until a shear rate of $60 \, \text{s}^{-1}$. At this shear rate, the viscosity becomes less than $9 \times 10^4 \, \text{Pa-s}$, which we hypothesize to be the threshold value till the microstructures breakdown occurs and the coating paste loses its elastic nature. Thus, at a higher shear rate, the material loses its integrity and a decrease in roughness was observed.

To more clearly demonstrate the relationship of the surface roughness with respect to capillary number and shear rate, a Peak Density Coefficient model (PDC) was used.

$$PDC = 2\dot{\gamma}C_aR(\frac{\eta}{\gamma})^{-0.7} \tag{6}$$

The PDC includes both the capillary number and shear rate ($\dot{\gamma}$) and was derived by observing how the PDC changes as peak density fluctuates. As seen in Fig. 7, the peak density has a linear relationship with the PDC .

Water Contact Angle Results

333334335

336

337

338

339

340

341

342

343

344

345

346

347

348

349

350

351

352

353

Fig. 8 shows the statistical plot of the WCA for each sample. The summary from the WCA experiment is reported in Table 3 and Fig. 9. Sample 4a had the highest WCA while sample 1c showed the lowest WCA. The average WCA was plotted for shear rate and capillary number in Fig. 9. This trend was very similar to the peak density and Wenzel roughness factor plots that are shown in Fig. 5. Since the superhydrophobicity depends on the peaks or textured surface of the sample, the WCA showed a very similar trend to the peak density plot shown in Fig. 5 (b). Thus, these WCA results validated both the surface descriptor and SEM results and aided in identifying the optimum conditions to fabricate a superhydrophobic, rough-textured surface. From the WCA results, we found that for a high contact angle, the range of capillary number should be from 4.5×10^5 to 6.0×10^5 and the shear rate should be from 40 s^{-1} to 60 s^{-1} . Almost all of the samples with capillary numbers around 5 x 10⁵ and shear rates greater than 40 s⁻¹ (Sample 2b, 3b, 4a) had high WCA values. It is important to note that fabricated samples exhibited hydrophobicity not superhydrophobicity; however, the trend of peak density with respect to the Capillary number and shear rate are promising to produce superhydrophobic samples. A smaller parameter sweep of both capillary number and shear rate to maximize peak density can be performed to maximize the WCA. Additionally, the viscoelastic material can be varied to achieve a maximized peak density and thus this manufacturing process has the potential to produce a surface that exhibits superhydrophobicity.

355356

354

CONCLUSION

Twelve samples with various shear rates and capillary numbers were fabricated using roll coating. The SEM, surface roughness, and the WCA for all these samples were analyzed to gain insight on the optimum process conditions to best mimic bioinspired, micro/nanotextured, rough surfaces. Thus, the critical factors involved in fabricating a rough-textured surface were identified and reported through this study. The optimum regions of the capillary number and shear rate were found and reported.

The capillary number should be in the range of 4.5×10^5 to 6.0×10^5 and the shear rate should be in the range of 40 s^{-1} to 60 s^{-1} . The introduction of the PDC model can be used to optimize operating parameters to finely tune surface roughness. The results from the SEM, surface descriptor, and the WCA found that samples 2b, 3a, and 4a showed a high rough optimum surface texture similar to the bioinspired surfaces. The sample with high roughness and a textured surface was obtained with a shear rate of 42.56 s^{-1} and a capillary number of 5.38×10^5 . All samples were hydrophobic with a maximum WCA of 128° . Thus, these two roll coating process parameters can be used to mimic bioinspired surfaces that are effective in superhydrophobic, self-cleaning, anticing, anti-biofouling, and drag reduction applications.

FUTURE SCOPE

In the current study, the two-roll coating process was effectively used to produce random, rough topography structures. All the samples produced in the optimum processing conditions were hydrophobic with a maximum WCA of 128°. The future

target of this study is to use the two-roll coating process, and the optimum parameters defined, to produce a desired topography surface that is superhydrophobic with a WCA greater than 150°. The next step in this direction will be to use other particle geometries (sphere, nano-rod, etc.) in the polymer composite. This will reduce the entanglement for uniformity of the coating surface. The nanoparticle wt % and other process parameters (i.e. roller distance) can be varied to reach the optimum condition. Additionally, this study focuses on the fundamental concepts present for roll-to-roll technology and in future work will be scaled up to a continuous web condition.

ACKNOWLEDGMENT

The efforts of this research were additionally supported by Dr. Yong Zhu and Yuxuan Liu of North Carolina State University.

FUNDING

This research is based upon work supported by the National Science Foundation (NSF) under grant no. 2031558. J. Ryu was also supported by the new faculty start-up fund at NC State University and the NCSU Faculty Research and Professional Development award. Part of this work was performed in part at the Analytical Instrumentation Facility (AIF) at North Carolina State University, which is supported by the State of North Carolina and the National Science Foundation (award number ECCS-2025064). The AIF is a member of the North Carolina Research Triangle Nanotechnology

- 403 Network (RTNN), a site in the National Nanotechnology Coordinated Infrastructure
- 404 (NNCI).
- 405

NOMENCLATURE

$\lambda_{Ribbing}$	ribbing wavelength
R	roller radius
d	roller gap
η	viscosity
γ	surface energy
U	roller speed
Са	Capillary number
Ca*	critical Capillary number
V	velocity
WCA	Water Contact Angle
G'	storage modulus
G''	loss modulus
LVR	Linear Viscoelastic Region
r	Wenzel roughness factor
Spd	peak density
Sdr	developed interfacial area ratio

409 **REFERENCES**

410

- 411 [1] Neinhuis, C., and Barthlott, W., 1997, "Characterization and Distribution of Water-
- 412 Repellent, Self-Cleaning Plant Surfaces," Ann. Bot., **79**(6), pp. 667–677.

413

- 414 [2] Cao, L., Jones, A. K., Sikka, V. K., Wu, J., and Gao, D., 2009, "Anti-Icing
- Superhydrophobic Coatings," Langmuir, **25**(21), pp. 12444–12448.

416

- 417 [3] Sun, T., Tan, H., Han, D., Fu, Q., and Jiang, L., 2005, "No Platelet Can Adhere-Largely
- 418 Improved Blood Compatibility on Nanostructured Superhydrophobic Surfaces," Small,
- 419 **1**(10), pp. 959–963.

420

- 421 [4] Sun, T., Feng, L., Gao, X., and Jiang, L., 2005, "Bioinspired Surfaces with Special
- 422 Wettability," Acc. Chem. Res., **38**(8), pp. 644–652.

423

- 424 [5] Vukusic, P., and Sambles, J. R., 2003, "Photonic Structures in Biology," Nature,
- 425 **424**(6950), pp. 852–855.

426

- 427 [6] Srinivasarao, M., 1999, "Nano-Optics in the Biological World: Beetles, Butterflies,
- 428 Birds, and Moths," Chem. Rev., **99**(7), pp. 1935–1961.

429

- 430 [7] Mainwaring, D. E., Nguyen, S. H., Webb, H., Jakubov, T., Tobin, M., Lamb, R. N., Wu,
- 431 A. H. F., Marchant, R., Crawford, R. J., and Ivanova, E. P., 2016, "The Nature of Inherent
- 432 Bactericidal Activity: Insights from the Nanotopology of Three Species of Dragonfly,"
- 433 Nanoscale, **8**(12), pp. 6527–6534.

434

- [8] Bhushan, B., 2012, "Adhesion of Multi-Level Hierarchical Attachment Systems in
- 436 Gecko Feet," https://doi.org/10.1163/156856107782328353, **21**(12–13), pp. 1213–
- 437 1258.

438

- 439 [9] Gao, X., and Jiang, L., 2004, "Water-Repellent Legs of Water Striders," Nature,
- 440 **432**(7013), p. 36.

441

- 442 [10] Liu, P., Gao, Y., Wang, F., Yang, J., Yu, X., Zhang, W., and Yang, L., 2017,
- 443 "Superhydrophobic and Self-Cleaning Behavior of Portland Cement with Lotus-Leaf-like
- 444 Microstructure," J. Clean. Prod., **156**, pp. 775–785.

445

- 446 [11] Yang, J., Long, F., Wang, R., Zhang, X., Yang, Y., Hu, W., and Liu, L., 2021, "Design of
- 447 Mechanical Robust Superhydrophobic Cu Coatings with Excellent Corrosion Resistance
- and Self-Cleaning Performance Inspired by Lotus Leaf," Colloids Surfaces A Physicochem.
- 449 Eng. Asp., **627**, p. 127154.

- 451 [12] Solutions, I., 2018, "Highly Wettable Slippery Surfaces: Self-Cleaning Effect and
- Mechanism," Int. J. Wettability Sci. Technol., 1, pp. 31–45.

- 454 [13] Hwang, H. S., Kim, N. H., Lee, S. G., Lee, D. Y., Cho, K., and Park, I., 2011, "Facile
- Fabrication of Transparent Superhydrophobic Surfaces by Spray Deposition," ACS Appl.
- 456 Mater. Interfaces, **3**(7), pp. 2179–2183.

457

- 458 [14] Kato, S., and Sato, A., 2012, "Micro/Nanotextured Polymer Coatings Fabricated by
- 459 UV Curing-Induced Phase Separation: Creation of Superhydrophobic Surfaces," J. Mater.
- 460 Chem., **22**(17), pp. 8613–8621.

461

- 462 [15] Zou, J., Chen, H., Chunder, A., Yu, Y., Huo, Q., and Zhai, L., 2008, "Preparation of a
- Superhydrophobic and Conductive Nanocomposite Coating from a Carbon-Nanotube-
- Conjugated Block Copolymer Dispersion," Adv. Mater., **20**(17), pp. 3337–3341.
- 465 [16] Lee, S., Lee, J., Park, J., Choi, Y., and Yong, K., 2012, "Resistive Switching WOx-Au
- 466 Core-Shell Nanowires with Unexpected Nonwetting Stability Even When Submerged
- 467 under Water," Adv. Mater., **24**(18), pp. 2418–2423.

468

- 469 [17] Zhu, L., Xiu, Y., Xu, J., Tamirisa, P. A., Hess, D. W., and Wong, C. P., 2005,
- 470 "Superhydrophobicity on Two-Tier Rough Surfaces Fabricated by Controlled Growth of
- 471 Aligned Carbon Nanotube Arrays Coated with Fluorocarbon," Langmuir, **21**(24), pp.
- 472 11208–11212.

473

- 474 [18] Liu, B., He, Y., Fan, Y., and Wang, X., 2006, "Fabricating Super-Hydrophobie Lotus-
- 475 Leaf-like Surfaces through Soft-Lithographic Imprinting," Macromol. Rapid Commun.,
- 476 **27**(21), pp. 1859–1864.

477

- 478 [19] Park, S.-H., Lee, S., Moreira, D., Bandaru, P. R., Han, I., and Yun, D.-J., 2015,
- 479 "Bioinspired Superhydrophobic Surfaces, Fabricated through Simple and Scalable Roll-
- 480 to-Roll Processing," Sci. Rep., **5**(1), p. 15430.

481

- 482 [20] Gurfinkel Castillo, M. E., and Patera, A. T., 1997, "Three-Dimensional Ribbing
- Instability in Symmetric Forward-Roll Film-Coating Processes," J. Fluid Mech., **335**, pp.
- 484 323-359.

485

- 486 [21] Chong, Y. H., Gaskell, P. H., and Kapur, N., 2007, "Coating with Deformable Rolls: An
- 487 Experimental Investigation of the Ribbing Instability," Chem. Eng. Sci., 62(15), pp. 4138–
- 488 4145.

489

- 490 [22] Bauman, T., Sullivan, T., and Middleman, S., 1982, "Ribbing Instability in Coating
- 491 Flows: Effect of Polymer Additives," Chem. Eng. Commun., **14**(1–2), pp. 35–46.

492

- 493 [23] Greener, J., Sullivan, T., Turner, B., and Middleman, S., 1980, "Ribbing Instability of
- 494 a Two-Roll Coater: Newtonian Fluids," Chem. Eng. Commun., 5(1–4), pp. 73–83.

495

496 [24] Yang, C. K., Wong, D. S. H., and Liu, T. J., 2004, "The Effects of Polymer Additives on

- the Operating Windows of Slot Coating," Polym. Eng. Sci., **44**(10), pp. 1970–1976.
- 498 [25] Bierwagen, G. P., 1992, "Film Coating Technologies and Adhesion," Electrochim.
- 499 Acta, **37**(9), pp. 1471–1478.

- 501 [26] Szczurek, E., Dubar, M., Deltombe, R., Dubois, A., and DUBAR, L., 2009, "New
- Approach to the Evaluation of the Free Surface Position in Roll Coating," J. Mater.
- 503 Process. Technol., **209**(7), pp. 3187–3197.

504

- 505 [27] Cohu, O., and Magnin, A., 1995, "Rheometry of Paints with Regard to Roll Coating
- 506 Process," J. Rheol. (N. Y. N. Y)., **39**(4), pp. 767–785.

507

[28] Brumm, P., Sauer, H., and Dörsam, E., 2019, "Scaling Behavior of Pattern Formation in the Flexographic Ink Splitting Process," Colloids and Interfaces, **3**(1), p. 37.

510

- [29] Pudas, M., Hagberg, J., and Leppävuori, S., 2005, "Roller-Type Gravure Offset
- 512 Printing of Conductive Inks for High-Resolution Printing on Ceramic Substrates," Int. J.
- 513 Electron., **92**(5), pp. 251–269.

514

- [30] Zevallos, G. A., Carvalho, M. S., and Pasquali, M., 2005, "Forward Roll Coating Flows
- of Viscoelastic Liquids," J. Nonnewton. Fluid Mech., **130**(2–3), pp. 96–109.
- [31] Fields, R. J., and Ashby, M. F., 1976, "Finger-like Crack Growth in Solids and Liquids,"
- 518 Philos. Mag., **33**(1), pp. 33–48.

519

- 520 [32] Grillet, A. M., Lee, A. G., and Shaqfeh, E. S. G., 1999, "Observations of Ribbing
- Instabilities in Elastic Fluid Flows with Gravity Stabilization," J. Fluid Mech., **399**, pp. 49–
- 522 83.

523

- 524 [33] Yamamura, M., 2020, "Ribbing Instability of Newtonian Fluid Coated on a
- 525 Topographic Surface," J. Coatings Technol. Res., **17**(6), pp. 1447–1453.

526

- 527 [34] Lee, J. H., Han, S. K., Lee, J. S., Jung, H. W., and Hyun, J. C., 2010, "Ribbing Instability
- 528 in Rigid and Deformable Forward Roll Coating Flows," Korea Aust. Rheol. J., 22(1), pp.
- 529 75–80.

530

- [35] Rosen, M., and Vazquez, M., 2007, "Secondary Waves in Ribbing Instability," AIP
- 532 Conference Proceedings, American Institute of PhysicsAIP, pp. 14–19.

533

- [36] Coyle, D. J., Macosko, C. W., and Scriven, L. E., 1990, "Reverse Roll Coating of Non-
- 535 Newtonian Liquids," J. Rheol. (N. Y. N. Y)., **34**(5), pp. 615–636.

536

- 537 [37] Varela López, F., Pauchard, L., Rosen, M., and Rabaud, M., 2002, "Non-Newtonian
- 538 Effects on Ribbing Instability Threshold," J. Nonnewton. Fluid Mech., 103(2–3), pp. 123–
- 539 139.

541 [38] Soules, D. A., Fernando, R. H., and Glass, J. E., 1988, "Dynamic Uniaxial Extensional 542 Viscosity (DUEV) Effects in Roll Application I. Rib and Web Growth in Commercial 543 Coatings," J. Rheol. (N. Y. N. Y)., 32(2), pp. 181–198. 544 545 [39] Coyle, D. J., 1997, "Knife and Roll Coating," Liquid Film Coating, Springer 546 Netherlands, Dordrecht, pp. 539–571. 547 548 [40] Shahsavar, A., and Bahiraei, M., 2017, "Experimental Investigation and Modeling of 549 Thermal Conductivity and Viscosity for Non-Newtonian Hybrid Nanofluid Containing 550 Coated CNT/Fe 3 O 4 Nanoparticles," Powder Technol., 318, pp. 441–450. 551 552 [41] Abbasi, S., Zebarjad, S. M., Baghban, S. H. N., Youssefi, A., and Ekrami-Kakhki, M.-S., 553 2016, "Experimental Investigation of the Rheological Behavior and Viscosity of 554 Decorated Multi-Walled Carbon Nanotubes with TiO2 Nanoparticles/Water Nanofluids," 555 J. Therm. Anal. Calorim., **123**(1), pp. 81–89. 556 557 [42] Jo, B., and Banerjee, D., 2014, "Viscosity Measurements of Multi-Walled Carbon 558 Nanotubes-Based High Temperature Nanofluids," Mater. Lett., 122, pp. 212–215. 559 560 [43] Islam, D., Perera, H., Black, B., Phillips, M., Chen, M.-J., Hodges, G., Jackman, A., Liu, 561 Y., Kim, C.-J., Zikry, M., Khan, S., Zhu, Y., Pankow, M., Ryu, J. E., Islam, M. D., Black, B., 562 Phillips, M., Chen, M.-J., Hodges, G., Liu, Y., Zikry, M., Zhu, Y., Pankow, M., Ryu, J. E., 563 Perera, H., Khan, S., Jackman, A., Micro, C.-J. K., and Lab, N. M., 2022, "Template-Free 564 Scalable Fabrication of Linearly Periodic Microstructures by Controlling Ribbing Defects 565 Phenomenon in Forward Roll Coating for Multifunctional Applications," Adv. Mater. 566 Interfaces, **9**(27), p. 2201237.

	Figure Captions List
Fig. 1	Schematic of two-roll coating machine with capillary bridging effect
Fig. 2	Rheology property of the 10% CNT - PDMS Paste
Fig. 3	Parameter plot to finalize process window
Fig. 4	Surface morphology of the 12 sample
Fig. 5	Variation of surface descriptors vs capillary number
Fig. 6	Variation of surface descriptors vs shear rate
Fig. 7	Peak Density Coefficient with respect to peak density
Fig. 8	Water contact angle results
Fig. 9	Variation of water contact angle vs capillary number and shear rate

Journal of Micro and Nano-Manufacturing

572573		Table Caption List			
	Table 1	Surface morphology of preliminary experiments			
	Table 2	Process parameters of the fabricated samples			
	Table 3	Roughness and WCA results of the samples			
574					

575 Figure List 576

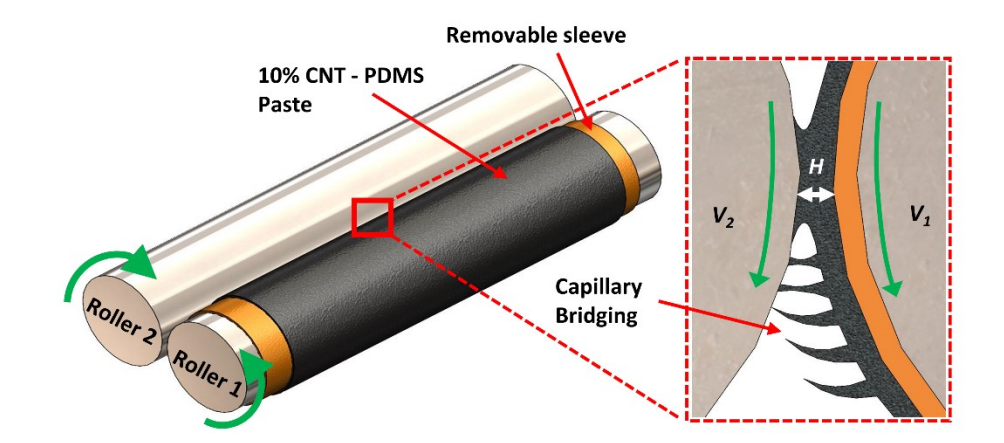


Fig. 1: Experimental set-up and visualization of the capillary bridging effect during forward roll-coating that develops the micro/nanostructures

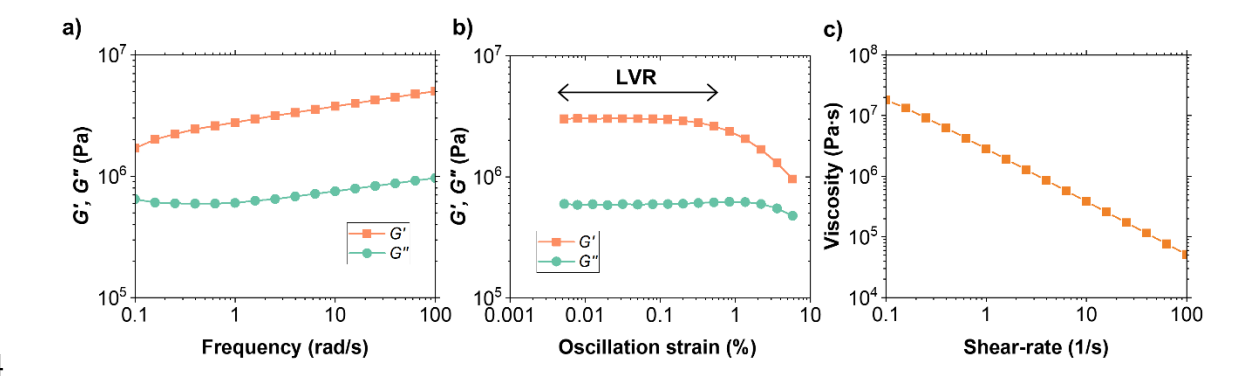


Fig. 2: (a) Storage and loss modulus at varying frequencies (b) The storage modulus and loss modulus of the CNT-PDMS paste as oscillations strain percentage increases with the Linear Viscoelastic Region (LVR) (c) The viscosity of the CNT-PDMS mixture as shear rate increases

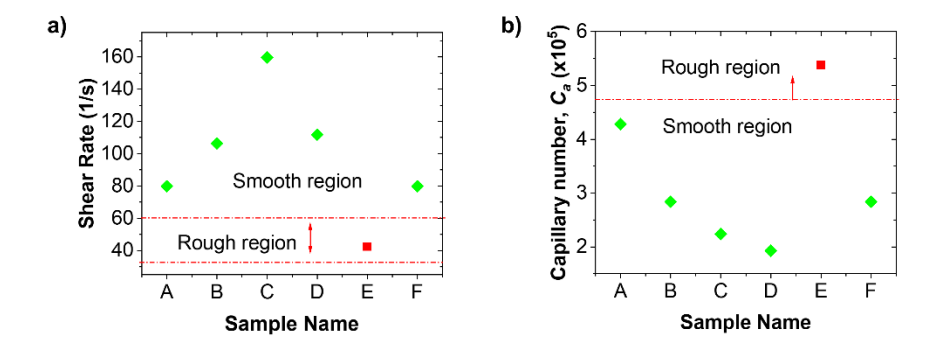


Fig. 3: (a) The shear rate of various samples and the identified process parameters of 20 s⁻¹ to 80 s⁻¹ (b) The capillary number for various samples and the onset of ribbing occurring above 4×10^5

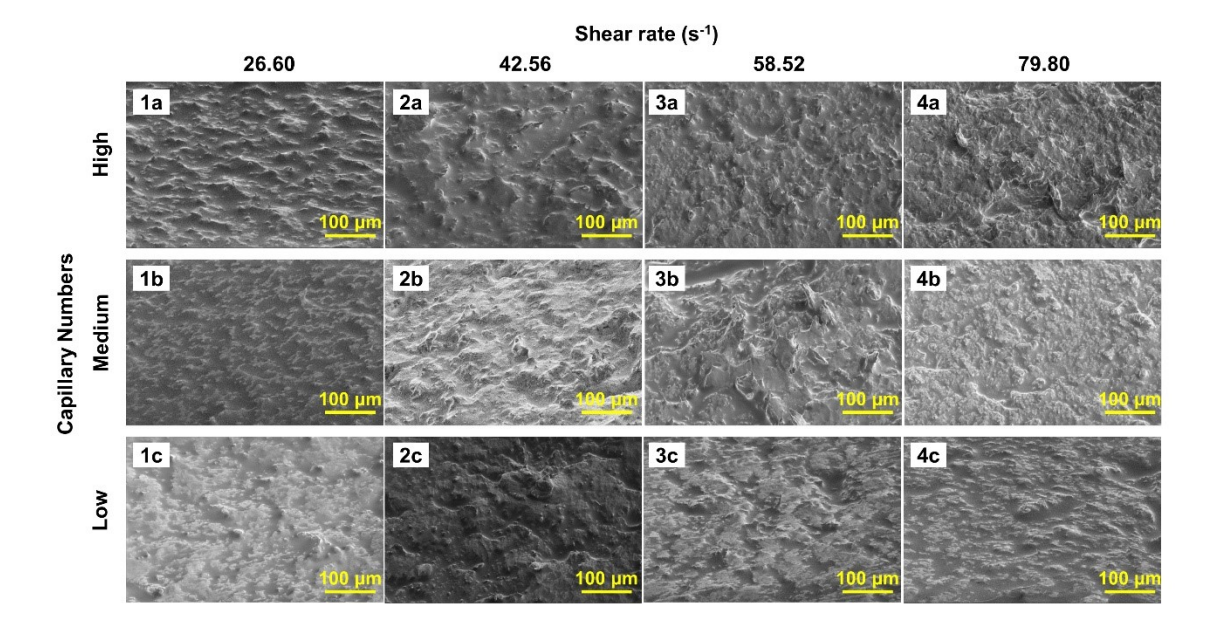


Fig. 4: Surface morphology of the respective samples in Table 2

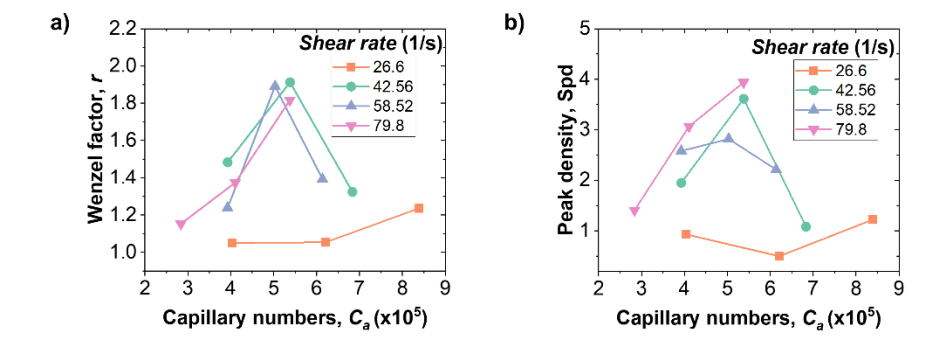


Fig. 5: (a) The variation of Wenzel roughness factor with respect to C_a for varying shear rates (b) Peak density in relation to capillary number for varying shear rates

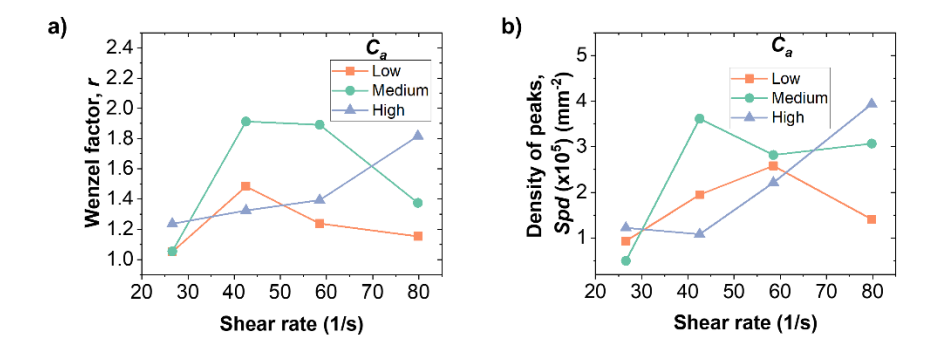


Fig. 6: (a) The variation of Wenzel roughness factor with respect to shear rate for varying Capillary numbers (b) Peak density in relation to shear rate for varying Capillary numbers

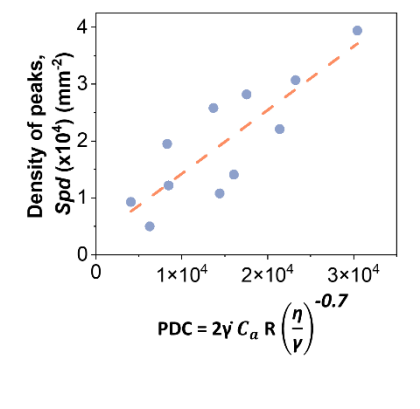


Fig. 7: The peak density of each sample plotted against the Peak Density Coefficient with a line of best fit to demonstrate linearity

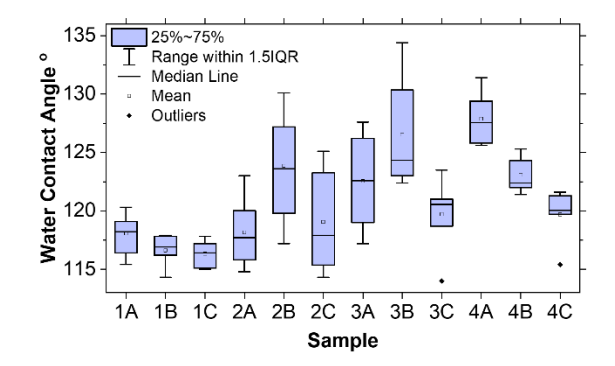


Fig. 8: WCA results for each respective sample outlined in Table 2

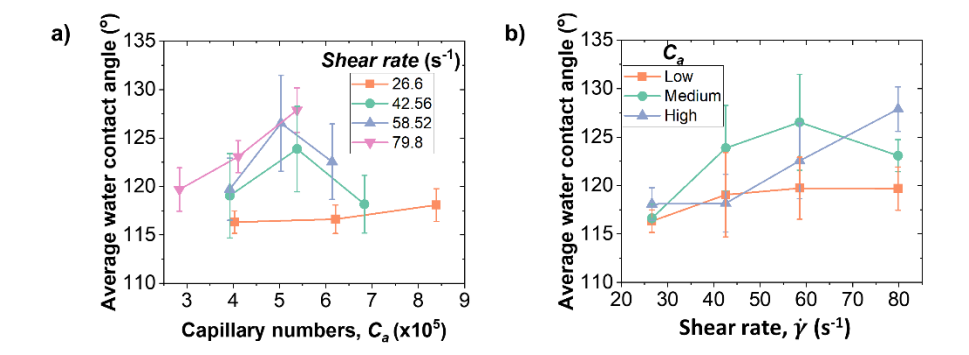


Fig. 9: Variation of WCA with respect to (a) Capillary number and (b) shear rate

634 Table List

Table 1: Forward roll-coating conditions, the material properties, and their respective surface morphology of preliminary experiments

Sample Name	<i>V</i> ₁ (rpm)	<i>V</i> ₂ (rpm)	Shear Rate (1/s)	Viscosity (Pa.s) (x10 ⁵)	Capillary Number (x10⁵)	SEM Image
А	43	58	79.80	0.69	4.28	75 µm
В	33	53	106.40	0.54	2.84	
С	33	63	159.59	0.38	2.24	
D	20	41	111.72	0.52	1.93	
E	33	41	42.56	1.19	5.38	
F	26	41	79.80	0.69	2.84	

 Table 2: Process parameters and material properties of the fabricated samples

Sample	V ₁	V ₂	V ₁	V ₂	Shear Rate	Viscosity	Capillary
Name	(rpm)	(rpm)	(cm/s)	(cm/s)	(s ⁻¹)	(x10 ⁵) (Pa-s)	Number (x10⁵)
1 a	36	41	9.58	10.91	26.60	1.79	8.39
1b	26	31	6.92	8.25	26.60	1.79	6.21
1c	16	21	4.26	5.59	26.60	1.79	4.03
2a	43	51	11.44	13.57	42.56	1.19	6.83
2b	33	41	8.78	10.91	42.56	1.19	5.38
2c	23	31	6.12	8.25	42.56	1.19	3.93
3a	50	61	13.30	16.23	58.52	0.91	6.14
3b	40	51	10.64	13.57	58.52	0.91	5.03
3c	30	41	7.98	10.91	58.52	0.91	3.93
4a	56	71	14.90	18.89	79.80	0.69	5.38
4b	41	56	10.91	14.90	79.80	0.69	4.11
4c	26	41	6.92	10.91	79.80	0.69	2.84

Table 3: Wenzel roughness factor, peak density, and average WCA of each respective samples

Sample Name	Wenzel Roughness Factor	Peak density (mm ⁻²) (x10 ⁴)	Avg. WCA (°)
1a	1.236	1.22	118.09
1b	1.054	0.50	116.62
1c	1.051	0.93	116.32
2a	1.324	1.08	118.17
2b	1.913	3.61	123.86
2c	1.483	1.95	119.05
3a	1.393	2.21	122.55
3b	1.891	2.82	126.53
3c	1.238	2.58	119.72
4a	1.817	3.94	127.88
4b	1.375	3.07	123.08
4c	1.153	1.41	119.68